metals

MDPI

Article

Microstructure Formation and Resistivity Change in CuCr during Rapid Solidification

Ulla Hauf [1,*], Alexander Kauffmann [1], Sandra Kauffmann-Weiss [2], Alexander Feilbach [3], Mike Boening [4], Frank E. H. Mueller [4], Volker Hinrichsen [3] and Martin Heilmaier [1]

1 Institute for Applied Materials (IAM-WK), Karlsruhe Institute of Technology (KIT), Engelbert-Arnold-Straße 4, 76131 Karlsruhe, Germany; alexander.kauffmann@kit.edu (A.K.); martin.heilmaier@kit.edu (M.H.)
2 Institute for Technical Physics (ITEP), Karlsruhe Institute of Technology (KIT), Hermann-von-Helmholtz-Platz 1, 76344 Eggenstein-Leopoldshafen, Germany; sandra.kauffmann-weiss@kit.edu
3 High Voltage Laboratories (HST), Technische Universität Darmstadt, Fraunhoferstr. 4, 64283 Darmstadt, Germany; feilbach@hst.tu-darmstadt.de (A.F.); hinrichsen@hst.tu-darmstadt.de (V.H.)
4 Plansee Powertech AG, Retterswil 13, 5703 Seon, Switzerland; mike.boening@plansee.com (M.B.); frank.mueller@plansee.com (F.E.H.M.)
* Correspondence: ulla.hauf@kit.edu; Tel.: +49-721-608-46556

Received: 5 October 2017; Accepted: 29 October 2017; Published: 4 November 2017

Abstract: The formation of the surface-near microstructure after a current interruption of CuCr contact materials in a vacuum interrupter is characterized by a fast heating and subsequently rapid solidification process. In the present article, we reveal and analyse the formation of two distinct microstructural regions that result from the heat, which is generated and dissipated during interruption. In the topmost region, local and global texture, as well as the resulting microstructure, indicate that both Cu and Cr were melted during rapid heating and solidification whereas in the region underneath, only Cu was melted and elongated Cu-grains solidified with the <001>-direction perpendicularly aligned to the surface. By analysing the lattice parameter of the Cu solid solution, a supersaturation of the solid solution with about 2.25 at % Cr was found independent if Cu was melted solely or together with the Cr. The according reduction of electrical conductivity in the topmost region subsequent to current interruption and the resulting heat distribution are discussed based on these experimental results.

Keywords: CuCr; supersaturation; solid solution; texture; powder metallurgy; microstructure; contact material; vacuum interrupter; heat affected volume

1. Introduction

CuCr is most commonly used as contact material for vacuum interrupters at medium voltage. For this application, the material system profits from a small solubility of Cr in Cu of maximum 0.82 at % in solid Cu at 1075 °C under equilibrium condition [1]. Hence, electrical and thermal conductivity of the alloys are only slightly decreased—mainly determined by the volume fraction of primary Cr-particles. For a Cu-alloy with 43 wt % Cr as a typical contact material, both elements form a homogenous liquid phase at temperatures between 1437 °C [2] and up to over 1800 °C [3,4], depending on the reference. In addition, several authors discussed a miscibility gap of the liquid phase [5,6]. For high cooling rates and low material purity, the miscibility gap is more likely and a homogenous liquid phase is expected only for higher temperatures. Since the alloys studied in this contribution are of commercial grade, such behaviour is expected.

In regular operating conditions in a vacuum interrupter, the sinusoidal current, with a peak current I_p, flows through the closed contacts. When the contacts are separated under load, current density

and thus joule heating increase until the contact material is melted and evaporated. If the current is interrupted, re-solidification occurs quickly. Detailed information about the fundamentals of vacuum interrupters and current interruption are given in Ref. [7]. After an interruption process, depending on the switching parameters, typical cathode and anode spots can be observed at the surface, which are reported by several authors [8–10]. The heat propagation into the depth was investigated in Ref. [10], where the microstructure and the heat affected volume (HAV) of disk shaped type as well as commercially used contacts was examined. The HAV of Cu with 25 wt % Cr and 43 wt % Cr was also investigated in a previous work [11]. For both compositions, HAV increases almost linearly and at similar slopes with rising transferred charge Q. It is generally smaller on the cathode. The results suggest that the chosen electrical parameters yield a well-defined material behaviour. Furthermore, a resistance increase of the contact material after a high-current interruption was discussed in Ref. [12]. However, the increase could not be linked to Cr in Cu solid solution due to the assumption that at maximum only 0.8 at % Cr can be dissolved while a supersaturation due to rapid solidification was not considered. Nevertheless, the details of microstructure formation and the impact of the according changes on the surface or surface-near properties remain inconclusive to date. Therefore, the aim of the present contribution is to clarify the origin of the observed microstructure and to link the results with temperature distribution and resulting electrical conductivity for future optimisation of contact materials. Furthermore, the impact of Cr-content is also investigated, which was not conclusively reported by authors in the past e.g., in Refs. [13–15].

2. Material and Methods

For the present contribution, two different alloys with 25 wt % and 43 wt % Cr, respectively, are compared. The contact materials were manufactured by powder metallurgy by Plansee Powertech AG (Seon, Switzerland) with an average Cr-particle size of about 40 µm. Cu- and Cr-powders (in commercial grades) were mixed, cold compacted and subsequently sintered under protective atmosphere, slightly below the melting point of Cu. The physical properties for the initial state were measured. Thermal diffusivity a was determined at 25 °C under vacuum (4×10^{-4} mbar) using a laser flash apparatus (LFA 427; Netzsch, Selb, Germany). The thermal conductivity λ was calculated using Equation (1), based on mass density ρ and specific heat capacity c according to an appropriate rule of mixture and the values provided in Ref. [16].

$$\lambda = a \cdot \rho \cdot c \tag{1}$$

The mass density ρ was measured according to Archimedes principle with a digital balance (Mettler AE 240). In addition, the heat capacity was confirmed by differential scanning calorimetry using a DSC 404 F1 Pegasus (Netzsch, Selb, Germany) under argon atmosphere. Electrical conductivity σ was determined at room temperature based on eddy currents (Sigmatest 2.069, Foerster, Reutlingen, Germany). Since penetration depth δ varies with frequency f according to Equation (2), f = 60 kHz was used for base material while it was increased to f = 960 kHz for assessing the material in the HAV subsequent to interruption.

$$\delta = \frac{1}{\sqrt{\pi \cdot f \cdot \sigma \cdot \mu_0}} \tag{2}$$

Thereby σ represents a homogeneous electrical conductivity of the probed material and μ_0 the magnetic vacuum permeability.

Microstructure, texture and lattice parameter were determined after rapid heating and solidification of CuCr caused by a current interruption, with an arcing time t_{arc}, a peak current I_p and a transferred charge Q, in a model vacuum chamber for disc shape contacts of 30 mm in diameter. The current interruption was performed with increasing sinusoidal current. The maximum contact velocity during current conduction within the first half-cycle was 2 m/s with a final contact gap of 11 mm. The chamber pressure was 2×10^{-6} mbar at maximum. Detailed information about the setup

of the model vacuum interrupter is reported in Ref. [17]. Characteristics and switching parameters for these two samples are shown in Table 1. In addition, a single-phase Cu-Cr reference alloy was produced by arc-melting, homogenisation at 1050 °C for 5 h and subsequent quenching in water. Scanning electron microscopic (SEM) analyses confirm a single-phase microstructure. The Cr-content of (0.72 ± 0.01) wt % was verified by inductively coupled plasma optical emission spectrometry (ICP-OES). This sample only serves as a reference for advanced characterisation and was not exposed to current interruption in the model vacuum interrupter.

Table 1. Characteristics of and switching parameters for the investigated contact material.

Alloy	Nominal Cr-Content in wt %	Nominal Cr-Content in at %	Nominal Cr-Content in vol %	Exp. Cr-Content in vol %	I_p in kA	t_{arc} in ms	Q in As
CC75	25	28.95	29.5	33 ± 2	6.25	10.4	43.6
CC57	43	47.97	48.5	53 ± 3	6.7	9.5	43.7
CuCr0.72	0.72 ± 0.01	0.89 ± 0.01		reference sample			

Sample preparation after single current interruption was performed perpendicular to the surface in the centre of the melted area. For optical microscope (OM) investigations and energy dispersive X-ray spectroscopy (EDX) analysis, cross sections were mechanically-chemically prepared and for OM subsequently etched using Beraha I solution. The experimental volume fraction of Cr in Table 1 was determined by area analyses at OM-micrographs. Cross sections for electron backscatter diffraction (EBSD) measurements were prepared by a standard metallographic procedure including grinding to a grid of P4000 and subsequent polishing with 1 µm suspension as well as oxide polishing suspension. For depth depending texture measurements via X-ray diffraction (XRD), target preparation by grinding was performed in order to remove 100 µm (CC57) as well as 140 µm (CC75) with respect to the surface.

As already mentioned, the HAV is more pronounced at the anode side. Therefore, texture analysis and EDX were performed on the anodes for the present contribution. EBSD was conducted on a Auriga cross-beam SEM (Carl Zeiss AG, Oberkochen, Germany) operated at 20 kV using an EDAX DigiView camera (AMETEK GmbH, Meerbusch, Germany). The orientation maps of 1000 µm × 350 µm were obtained by indexing patterns with eight to ten bands at a point rate of about 125 s^{-1} and a step size of 0.5 µm. The fraction of indexed points is above 99.8%. XRD texture measurements were carried out on a Bruker D8 diffractometer equipped with an Eulerian cradle (Bruker AXS GmbH, Karlsruhe, Germany). The Cu X-ray tube was operated at 40 kV and 40 mA. A Göbel mirror, a circular slit of 1 mm in diameter and a 1 mm collimator were used at the source as well as two motorized slits of 9 mm at the LynxEye-XE detector (Bruker AXS GmbH, Karlsruhe, Germany) in 0 D mode with three channels. Three pole figures, namely {111}, {200} and {220} for Cu, were determined between 0° to 360° in Φ as well as 0° to 80° in Ψ in steps of 4°. The defocusing-induced intensity decrease with increasing tilt angle was quantitatively determined on non-textured Cu-powder samples produced by sedimentation. Recalculation of the orientation distribution function (ODF) was performed utilising the MTEX toolbox 3.5.0 in conjunction with Matlab R2014a [18]. For lattice parameter determination, XRD was carried out on a D2 Phaser system by Bruker equipped with a LynxEye detector (Bruker AXS GmbH, Karlsruhe, Germany). The Cu X-ray tube was operated at 30 kV and 10 mA. The according lattice parameter was determined by extrapolating towards $\theta = 90°$ using the following weighting function according to Nelson-Riley $\frac{1}{2}(\cot^2\theta + \cot\theta \times \cos\theta)$ with a 95% confidence interval. Furthermore, EDX was conducted on a Zeiss Leo EVO 50 scanning electron microscope (SEM; Carl Zeiss AG, Oberkochen, Germany) at an acceleration voltage of 25 kV equipped with a Thermo Fisher Scientific SDD detector (Thermo Fisher Scientific, Waltham, MA, USA) for composition determination.

3. Results and Discussion

3.1. Microstructure

The following investigations were performed on an anode of CC57 and CC75 (Table 1). A cross section of the anode side of CC75 after single switching with I_p = 6.25 kA, t_{arc} = 10.4 ms and Q = 43.6 As, is exemplarily shown in Figure 1. The OM micrographs reveal the formation of two distinct zones with significantly different morphologies: (i) In Region 1 (R1) a high amount of fine Cr-particles (about 450 nm by SEM investigations) are observed beside few larger Cr-particles (see the magnified detail in Figure 1b); (ii) Region 2 (R2) contains Cu-grains, which are elongated and perpendicularly aligned to the surface. In addition, Cr seems not to be affected by the dissipated heat here. Below R2 both phases remain virtually unaffected, thus remaining in the initial state. The zone formation is similar to the observations reported in [10] for Cu-43 wt % Cr contact material from a commercial vacuum interrupter.

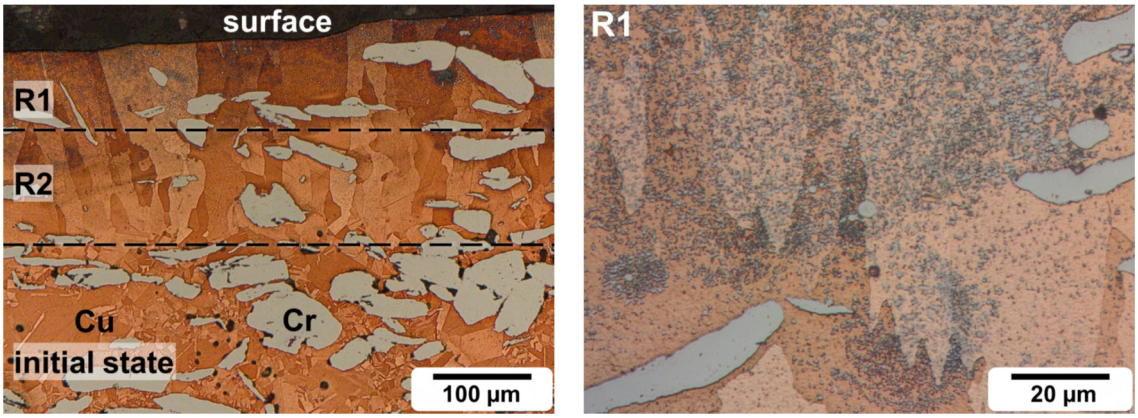

(**a**) (**b**)

Figure 1. Optical micrographs of a cross section on the anode of CC75 subsequent to single current interruption (I_p = 6.25 kA, t_{arc} = 10.4 ms, Q = 43.6 As). (**a**) R1 and R2 indicate two distinct regions with significantly different morphology; (**b**) Magnified section of R1.

The same investigations are also performed for CC57. Similar microstructures can also be found for CC57 and therefore are not shown in this paper. The depths of the heat affected regions were determined in a statistically relevant way and are summarised for CC57 and CC75 in Table 2. While R1 is slightly more extended for CC75 than for CC57, the reverse trend is observed for R2.

Table 2. Depths of R1 and R2 for CC75 and CC57 on anode side.

Alloy	Depth of R1/µm	Depth of R1 + R2/µm
CC75	101 ± 9	170 ± 12
CC57	81 ± 9	219 ± 22

As compared to the initial Cr-particle size of about 40 µm, the observed very fine Cr-particles in R1 strongly indicate the solidification from the melt of both Cu and Cr. The resulting average Cr-particle size (equivalent diameter was investigated with SEM) on the surface is 530 nm for CC75 and 432 nm for CC57, respectively (However, there is no general correlation (neither to composition nor to Q) with the resulting Cr-particle size). Thus, the cooling rates must have been very high and were estimated to be approximately 5×10^4 to 2×10^5 K/s for particle sizes between 100 and 500 nm according to Refs. [19,20]. In contrast to the morphology in R1, which suggests a formation from the liquid of both Cu and Cr, the appearance of the elongated Cu-grains in R2 remains unclear.

Both a solid state directional recrystallization as well as a solidification of Cu only are possible. In both cases, characteristic, crystallographic texture should be obtained. Hence, texture with respect to the anticipated temperature gradient is analysed in the following.

3.2. Local Texture Analysis

Figure 2 presents phase information, image quality and orientation maps of Cu obtained by EBSD on cross sections of CC57 and CC75, respectively, subsequent to a single switching operation. The different volume fractions of Cr of the initial material are obvious when comparing the phase maps. In addition, R1 where both Cr and Cu have presumably been in the liquid phase during switching can also be identified due to the Cr-particles in the range of several hundred nanometres (highlighted with arrows in Figure 2) in comparison to the Cr in R2 remaining virtually unaffected. This is even more evident when comparing image quality maps (IQ). Correct indexing of the entire amount of small Cr-particles might be difficult due to the limited probe size of EBSD. In R1, image quality is significantly reduced due to the large amount of small Cr-particles (dark grey colour). Within both regions, elongated Cu-grains can clearly be identified in the orientation map (highlighted with dotted lines as example for CC75) whereas Cu exhibits globular grains in the base material. The black area in all three images of CC57 is expected to be a preparation artefact.

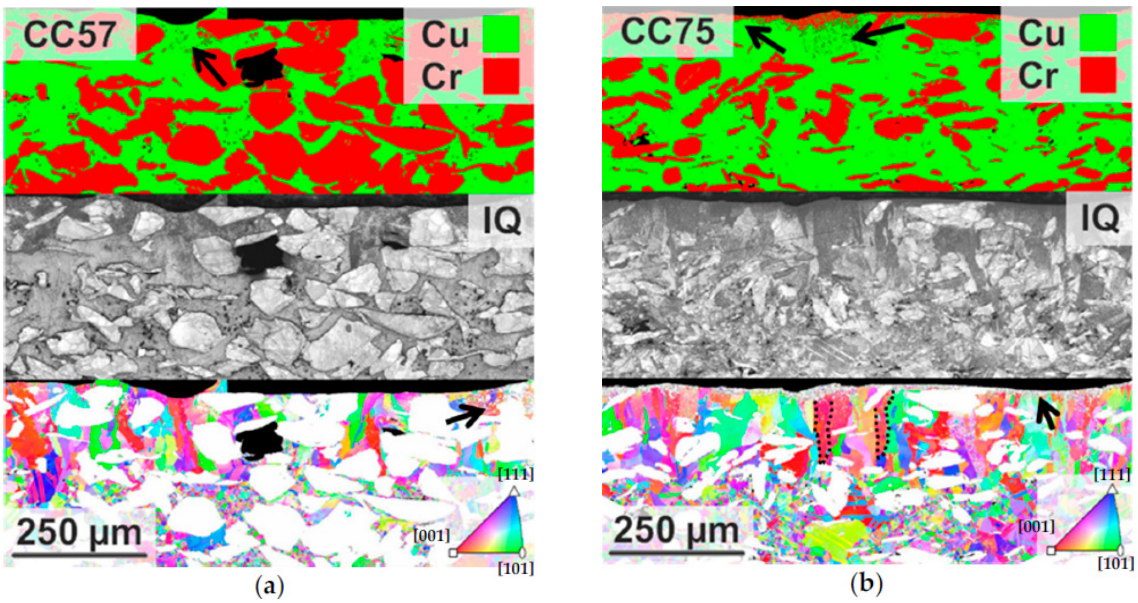

Figure 2. CC57 (**a**) and CC75 (**b**). From top to bottom: phase information (Cu and Cr are colour coded in green and red, respectively), image quality (IQ) and orientation of Cu (colour-code corresponds to the inverse pole figure of the surface normal; inset). Arrows indicate small Cr-particles solidifying from the liquid after switching. Dotted lines highlight elongated grains.

In the case of a crystallisation from the liquid, characteristic solidification texture for cubic metals is expected. A fibre texture with <001> (crystallographic equivalent directions to [001]) parallel to the solidification direction can typically be found [21]. In the present case, the temperature gradient, the according heat dissipation and, thus, the solidification direction are expected to be perpendicular to the surface. For this reason, the orientation maps for Cu are colour-coded according to the inverse pole figure of the sample surface normal. The anticipated texture component corresponds to red colour within the standard triangle in the inset. The statistics of texture components in Figure 3 are determined by cropping of the distinct regions in the EBSD maps based on the depths presented in Table 2. In both cases, comparably strong <001> fibre texture components in R1 as well as in R2 provide evidence that Cu was in liquid state and solidified with the characteristic texture component. For CC57,

the <001> fibre texture component is comparably strong and sharp in R1 (multiples of the uniform distribution (mud) of 4.3) in comparison to the preferential orientation in R2 (2.42 mud). In case of CC75, texture is not that strong but still significant.

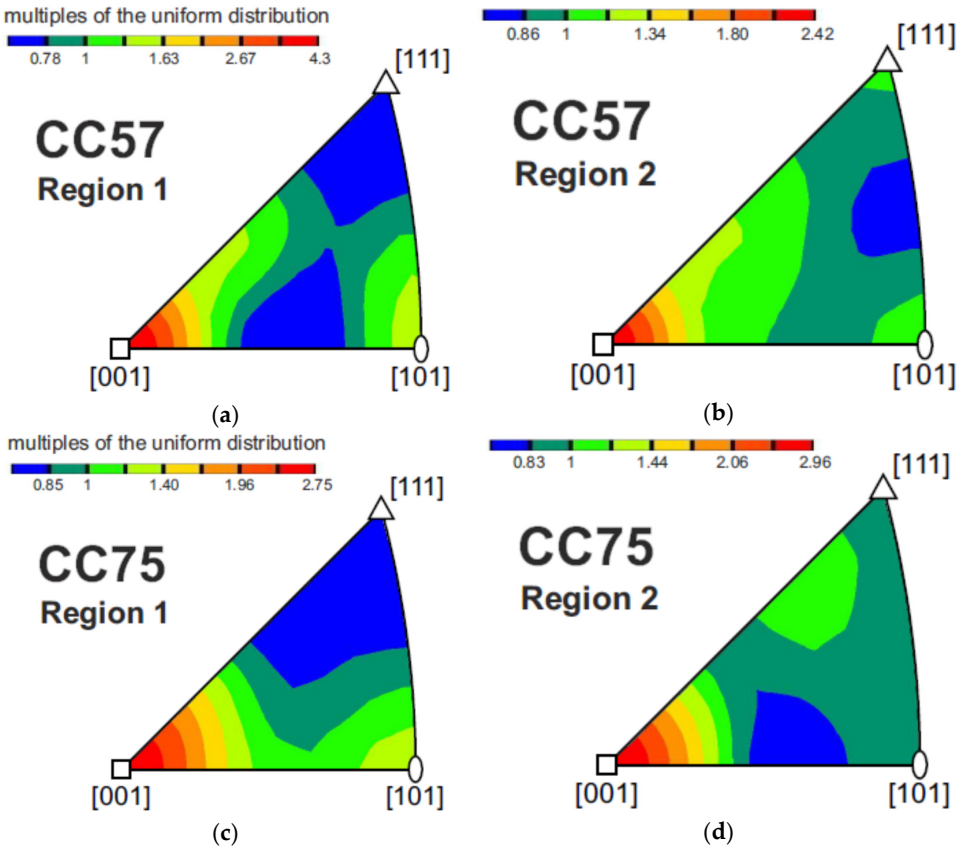

Figure 3. Orientation distribution functions within the standard triangle for the inverse pole figure of the sample surface normal for cropped EBSD (electron backscatter diffraction) maps from R1 and R2 (Figure 3a,c and Figure 3b,d, respectively) in CC57 and CC75 (Figure 3a,b and Figure 3c,d, respectively).

3.3. Global Texture Analysis

In order to verify the local texture results with significant statistics of analysed grains, global texture was determined for the base material, the thermally stressed surface (R1) as well as for material with target preparation to R2. The results are presented in Figure 4. For the initial material, only minor texture is expected due to the uniaxial pressing of the powder metallurgical processing. In this case, a <101> fibre texture component parallel to the compression direction is expected for Cu [20]. Since the compression direction coincides with the sample surface normal of the tested contacts, slight preferential orientation with <101> parallel to the surface normal can be identified in both initial states. Nevertheless, strength and sharpness of this texture component remain weak and broad (<<1.5 mud). In accordance with the local texture observations, typical solidification textures with <001> fibre texture are observed after single current interruption underneath the surface. In contrast to the EBSD results, Figure 4 depicts texture analysis with a significantly larger number of determined grains whereas statistics in Figure 3 can be dominated by single grains with comparably large fraction within the EBSD scan area. Thus, strength and sharpness of the texture components are more reliable in comparison to Figure 3. For CC57, a significantly lower strength of the <001> fibre texture component is observed in comparison to CC75 (2.6 mud vs. 8.6 mud, respectively). This might be attributed to the details of the heat dissipation in both materials. Texture is caused by either preferential nucleation of new grains or preferential growth of existing nuclei [22]. For rapid growth conditions, textured, columnar

grains are likely and the observation of elongated Cu-grains in the present case can be attributed to such solidification conditions. Six major parameters are known to influence these conditions: (i) superheating; (ii) cooling rate; (iii) thermal gradient; (iv) solid-liquid interface; (v) mold materials and (vi) solute concentration [23] of which most parameters are interdependent. If superheating increases, texture development typically decreases [23]. For nickel-base super alloys, it was found that higher cooling rates lead to sharper textures [24]. For the formation of the microstructure after a single current interruption under vacuum in the present case, the superheating, cooling rate and thermal gradient might be the dominant parameters affecting texturing. Due to different compositions of the two investigated alloys and therefore different thermal conditions, it is obvious that sharpness of texture might be different. While melting temperature of both alloys are almost similar (1400 °C for CC75 and 1435 °C for CC57) [2], electrical ($\sigma_{\mathrm{eff}}^{\mathrm{bulk}}$) and thermal conductivity (λ_{CC75} = (252 ± 28) W/(m·K) and λ_{CC57} = (192 ± 7) W/(m·K) at 25 °C) vary. On the one hand, a higher electrical conductivity (of CC75) leads to enhanced joule heating and therefore might cause higher overheating. On the other hand, the higher thermal conductivity of CC75 might lead to higher cooling rates and thus reduce the superheating. Given that texture is stronger for CC75, it is concluded that the solidification process after current interruption is dominated by the higher cooling rates of CC75. This has to be carefully reviewed using specific simulations in future. For R2, weaker texture strength is observed compared to R1, which might be correlated to a lower superheating. Due to target preparation and the inhomogeneity of depth of R1 and R2, a portion of R2 is already removed as well. Therefore, a considerable portion of base material already contributes to the orientation distribution. This is further proven by the upcoming <101> fibre texture which stems from the initial material.

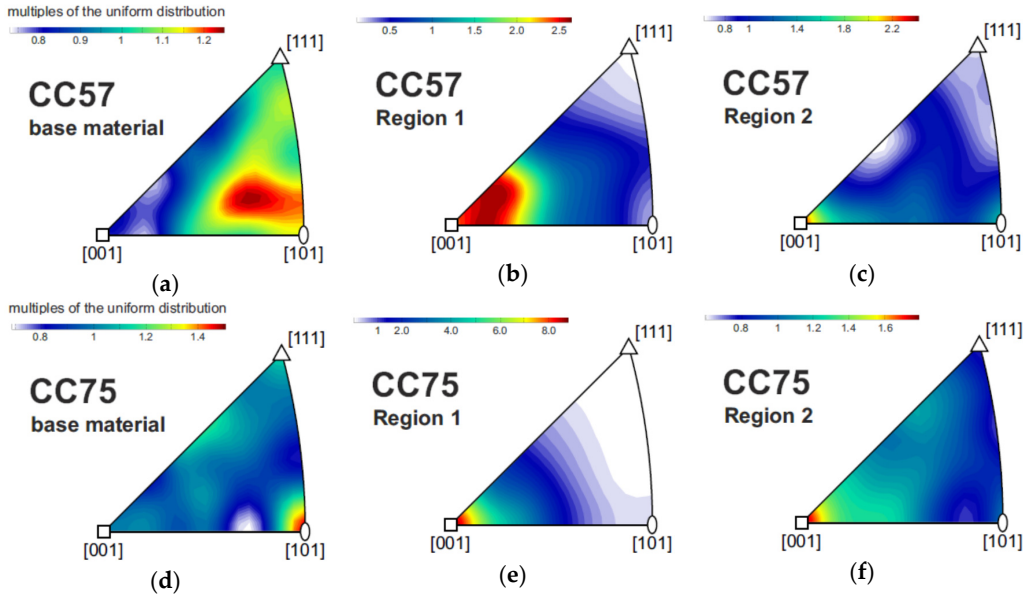

Figure 4. ODF (orientation distribution function) calculated by using global texture data presented within the standard triangle for the inverse pole figure of the sample surface normal in CC57 and CC75 ((**a**–**c**) and (**d**–**f**), respectively). Texture was determined for the initial material, R1 and R2, respectively (from (**a**,**d**) to (**c**,**f**)).

3.4. Cr-Content in the Cu Solid Solution

Based on the high cooling rates, it is expected that Cr can be solved and in some cases supersaturated in the Cu solid solution (denoted by (Cu)). This was investigated by means of XRD measurements. The lattice parameters *a* of (Cu) before and after switching operation were calculated by extrapolation of all obtained peaks and compared to literature data. According to Tenwick and Davies [25], and Bell and Davies [26], *a* increases with increasing Cr-content by 0.0023 to 0.0025 Å/at %

up to a Cr-content of about 4–5 at %. Thus, the average value of 0.0024 Å/at % is used in the following for the re-calculation of the dissolved Cr-content in (Cu) (denoted by $X_{Cr}^{(Cu)}$) and plotted in Figure 5. The lattice parameter for pure Cu has been additionally determined on a powder reference sample and the obtained value of 3.6150 Å is in good agreement with literature data [27]. Error bars correspond to the standard deviation for the initial materials of at least three samples per alloy and to the 95% confidence interval of the utilised extrapolation method for samples subsequent to interruption due to limited sample volume. Literature data are taken from Refs. [25,26] (full squares and diamonds). The dependence of the lattice parameter on the dissolved Cr-content has been verified by the reference sample CuCr0.72 (open diamond symbol).

The initial states (open circle and triangle) of the investigated contact materials already exhibit an increased lattice parameter in comparison to pure Cu. This indicates a small amount of 0.1–0.3 at % dissolved Cr, which might be attributed to the heat treatment at elevated temperatures for sintering during manufacturing. Sample variation is small in comparison to the supersaturation effect described in the following. After single current interruption, the lattice parameter increased and therefore the amount of dissolved Cr in (Cu) has to be about 2–2.5 at % Cr (half-filled symbols). There is no evidence for significant differences between CC57 and CC75. Removal of R1 in order to gain sole information from R2 did not lead to significant changes of these findings. This further proves that Cu was melted in R2 during the interruption process. For this reason, the degree of supersaturation of Cr is similar to that in R1.

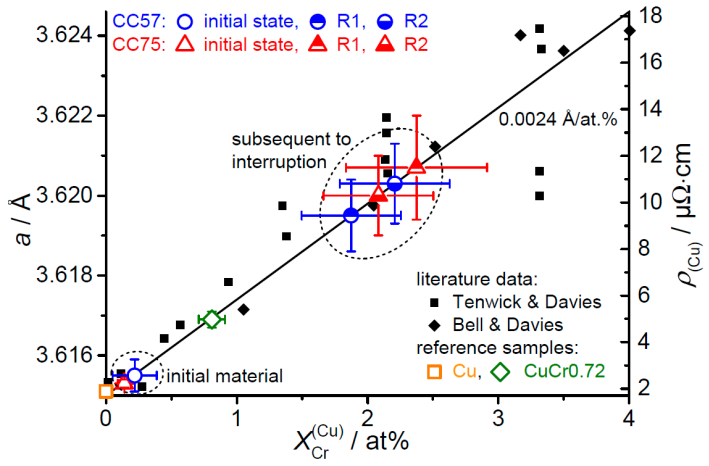

Figure 5. Lattice parameter *a* and electrical resistivity of (Cu) $\rho_{(Cu)}$ ($\rho_{(Cu)} = 1.71 + 4.12\,\frac{\mu\Omega\cdot cm}{at\ \%} \times X_{Cr}^{(Cu)}$ [25]) as a function of dissolved Cr in (Cu) $X_{Cr}^{(Cu)}$. Literature data are taken from Tenwick and Davies [25], and Bell and Davies [26].

3.5. Propagation of Cr-Content $X_{Cr}^{(Cu)}$ into the Depth

To clarify the propagation of $X_{Cr}^{(Cu)}$ into the depth, the results were compared to EDX spot measurements (Figure 6). The spot was placed on an area where only Cu matrix was observed. $X_{Cr}^{(Cu)}$ was determined as depth profile for CC57 and CC75. For both investigated compositions, EDX measurements show a decreasing Cr-content with increasing distance to the surface (Figure 6). The high $X_{Cr}^{(Cu)}$ up to 100 µm compares well to the depth of R1 determined by OM (see Table 2) while EDX-measurements reveal a slightly lower Cr-content for distances between 100 µm and 200 µm, which corresponds to R2. This is in contrast to the lattice parameter dependency in Figure 5 where R1 and R2 incorporate the same amount of Cr in (Cu). Thus, the depth-dependence of $X_{Cr}^{(Cu)}$ determined by EDX is supporting the differences between R1, R2 and the base material as determined by OM (see Table 2).

The results were further proven by analysing the reference sample CuCr0.72 (with 0.89 at % Cr). A slightly overestimated Cr-content of (0.96 ± 0.04) at % was determined. In general, the Cr-content, measured by EDX within R1, has to be treated with care due to the high excitation volume at 25 kV and the Cr-particle size and density. It is assumed that sub-surface and adjacent Cr-particles may increase the determined Cr-content in (Cu). However, full excitation of the analysed X-ray lines for proper composition analysis requires the chosen acceleration voltage. This leads to much higher $X_{\mathrm{Cr}}^{(\mathrm{Cu})}$ in R1 compared to the lattice parameter dependency in Figure 5.

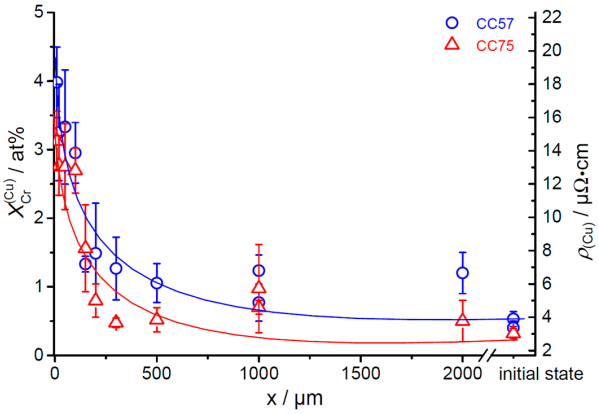

Figure 6. Development of Cr-content $X_{\mathrm{Cr}}^{(\mathrm{Cu})}$ and electrical resistivity of (Cu) $\rho_{(\mathrm{Cu})}$ ($\rho_{(\mathrm{Cu})} = 1.71 + 4.12 \frac{\mu\Omega\cdot\mathrm{cm}}{\text{at \%}} \times X_{\mathrm{Cr}}^{(\mathrm{Cu})}$ [25] as a function of distance from the surface x for CC57 and CC75 with standard deviations of at least five individual EDX (energy dispersive X-ray spectroscopy) spot measurements, curves are plotted to guide the eyes.

3.6. Influence on Electrical Conductivity

Electrical conductivity is one key parameter determining the performance of contact materials under normal operation conditions. Based on the aforementioned microstructural results, it is assumed that the electrical conductivity σ in the bulk material as well as in R1 and R2 is significantly decreased by incorporation of Cr into (Cu). In the following, the electrical conductivity is therefore tracked on the basis of the microstructural results determined in the previous sections.

For the theoretical assessment, two contributions to electrical conductivity have to be considered: (i) the volume fraction of Cr-particles f_{Cr} and of the solid solution $f_{(\mathrm{Cu})}$ within the compound as well as (ii) the reduced electrical conductivity $\sigma_{(\mathrm{Cu})}$ of the solid solution (Cu). The electrical conductivity of Cr is assumed to be unaffected by the switching process or by microstructural conditions (σ_{Cr} = 8 MS/m at room temperature [28]). The volume fraction of Cr-particles f_{Cr} in R1 is unknown and assumed to correspond to the bulk value of the initial materials.

Since the investigated alloys are macroscopically almost homogeneous with spherical Cr-particles (see Figure 2), the corresponding case in Hashin-Shtrikman formalism [29] is used to calculate the effective electrical conductivity σ_{eff} of the compound materials (Equation (3)):

$$\sigma_{\mathrm{eff}} = \sigma_{(\mathrm{Cu})} + \frac{f_{\mathrm{Cr}}}{\frac{1}{\sigma_{\mathrm{Cr}} - \sigma_{(\mathrm{Cu})}} + \frac{f_{(\mathrm{Cu})}}{3\sigma_{(\mathrm{Cu})}}} \tag{3}$$

Figures 5 and 6 already indicate the increasing electrical resistivity $\rho_{(\mathrm{Cu})}$ with increasing Cr-content in (Cu) $X_{\mathrm{Cr}}^{(\mathrm{Cu})}$. This is based on Ref. [25], where a base resistivity of pure copper of 1.71 μΩ·cm was determined which increases with 4.12 μΩ·cm/at % Cr since Cr atoms act as efficient scattering centres. For the final assessment, $\sigma_{(\mathrm{Cu})}$ according to Figure 5 was used since XRD provides information of a rather large proportion of the material. The calculated electrical conductivity of (Cu) in the initial state ($\sigma_{(\mathrm{Cu})}^{\mathrm{bulk}}$) and in R1 ($\sigma_{(\mathrm{Cu})}^{\mathrm{R1}}$) are presented in Table 3. Uncertainties are calculated with respect to the

error bars for lattice parameter measurement (Figure 5). Since $\sigma_{(Cu)}$ is non-linearly depending on $X_{Cr}^{(Cu)}$, uncertainties in $\sigma_{(Cu)}$ for small Cr-contents (as in bulk material) are higher than for high Cr-contents (as in R1). The applied method and literature data were further validated using the CuCr0.72 sample which has an electrical conductivity of $19.9^{+1.9}_{-1.6}$ MS/m on the basis of its lattice parameter which is in very good agreement with the experimentally determined value of (20.87 ± 0.01) MS/m.

Table 3. Calculated $\sigma_{(Cu)}$ for bulk material and R1 for CC57, CC75 and CuCr0.72, respectively.

Sample	$\sigma_{(Cu)}^{bulk}$/MS/m	$\sigma_{(Cu)}^{R1}$/MS/m
CC57	$38.4^{+14.6}_{-8.3}$	$10.6^{+2.1}_{-1.5}$
CC75	$43.8^{+4.5}_{-3.8}$	$8.7^{+2.1}_{-1.5}$
CuCr0.72	$19.9^{+1.9}_{-1.6}$	-

The calculated electrical conductivities σ_{eff}^{bulk}, of the bulk materials in the initial state are presented in Figure 7 as a function of the according volume fraction of Cr-particles. Obviously, a significantly reduced electrical conductivity of the solid solution leads to a substantial reduction of the electrical conductivity in the compound material already in the as-manufactured condition. For comparison, a calculation assuming no incorporation of Cr in Cu (58.36 MS/m) is presented to highlight this effect. A comparison of the calculation with the experimental values obtained for CC57 and CC75 in Table 4 reveals good agreement.

Table 4. Determined electrical conductivity of bulk material and (mostly) R1 as well as the penetration depth at 960 kHz (with σ_{eff}^{R1}) for CC57 and CC75.

Sample	σ_{eff}^{bulk}/MS/m	σ_{eff}^{R1}/MS/m	Penetration Depth at 960 kHz/µm
CC57	21.7 ± 0.4	7.3 ± 0.1	190
CC75	31.5 ± 0.2	10.6 ± 0.1	158
CuCr0.72	20.87 ± 0.01	-	-

The major uncertainty of the calculation stems from the experimental uncertainty of the re-calculation of the dissolved Cr-content. This is directly translated to the uncertainty of the re-calculated Cr-content and the according expectation interval is visualised by shaded areas in Figure 7.

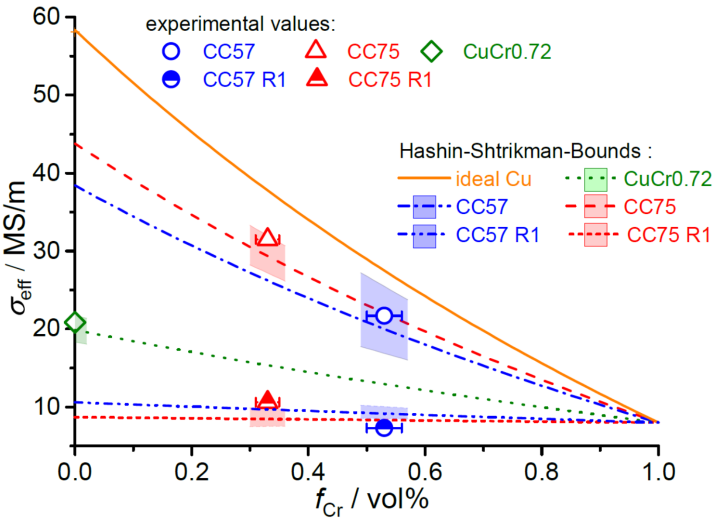

Figure 7. Comparison of experimentally observed and calculated electrical conductivities. Calculated σ_{eff} with σ_{Cu} = 8 MS/m and $\sigma_{(Cu)}$ according to Table 3. Errors of experimentally determined σ are below the symbol size.

The supersaturation of Cr in the matrix by the switching process further reduces the electrical conductivity in the topmost layers of the switched materials ($\sigma_{\mathrm{eff}}^{\mathrm{R1}}$). The experimental assessment of the electrical conductivity of this surface near region is more challenging in comparison to that for the bulk materials. In the present investigation, an increased frequency of 960 kHz for a reduction of the penetration depth was applied. The determined depths (estimated by using $\sigma_{\mathrm{eff}}^{\mathrm{R1}}$) are included in Table 4. When applying the aforementioned method, attention has to be paid to larger experimental errors due to increasing surface roughness subsequent to switching event compared to initial material. Thus, a further increased frequency (for further reduction of the penetration depth) does not seem to be reasonable in the present case. Though the probe volume of the electrical conductivity measurement is not fully consistent with the extent of R1, a good agreement between the measured surface near electrical conductivity (half-filled triangle and circle in Figure 7) and the calculated electrical conductivity according to Equation (3) (lines in Figure 7) is observed. As in the case of the bulk material, the experimental uncertainty in measuring the dissolved Cr-content mainly determines the uncertainty of the predicted electrical conductivity and is highlighted by the shaded areas. Moreover, the assumption of aforementioned constant volume fraction of Cr-particles seems to be disputable. On the one hand, the volume fraction of small Cr-particles remains unknown and might be different from the one expected for the bulk material. On the other hand, displaced (within the molten material during switching) or clustered Cr-particles are frequently observed causing inhomogeneous electrical properties. Further microstructural parameters which might also contribute to a decreasing electrical conductivity like phase boundaries, porosity and impurities were discussed in Ref. [30]. Nevertheless, the present contribution shows that the altered electrical conductivity predominantly arises from the Cr-content supersaturated in Cu solid solution.

The application of CuCr contact material in vacuum interrupters leads to a significantly reduced electrical conductivity, at least under the present operating conditions. Consequently, this reduces the efficiency of current conduction during normal operation. Vacuum interrupters are complex electrical engineering systems and the present contribution focuses only on one of the contributing effects. In reality, for the whole electrical system, other factors have to be considered as well. Nevertheless, the assessment of individual effects under reproducible conditions will play an important role for further development of vacuum interrupters.

The problem of reducing electrical conductivity of the molten volume might be addressed by using alloying elements with even lower or virtually no solubility in Cu, e.g., Vanadium (maximum solubility in solid solution 0.17 at % [31]). As reported in Ref. [26], the maximum supersaturation of V in Cu is only 1 at % (compared to 4–5 at % Cr). Thereby, resistivity of Cu-V only increases by 8.6 μΩ·cm [26] compared to Cu-Cr, which increases by 20.6 μΩ·cm [25] at maximum. However, electrical conductivity of V is below that of Cr. Therefore, the possible benefit of such materials will depend on the initial volume fraction of V versus the exact amount of supersaturated V in (Cu) after a potential switching operation. Of course, further physical parameters, such as vapour pressure, melting point of the alloying element and resulting erosion as well as welding behaviour of the alloy can dominate the process of current interruption and have also been taken into account. Furthermore, the significance of the reduction of the electrical conductivity after switching operation must be worked out in detailed electrical engineering studies in the future.

3.7. Heat Distribution

By combining the above results, the temperature development into the depth of the contact electrode can be estimated. From microstructural (Figure 1) and texture analysis (Figures 3 and 4), it is proven that in R1 both Cu and Cr were melted during interrupting process. This indicates temperatures exceeding 1800 °C. This is consistent with several authors' findings who reported surface temperatures above 2000 °C [32,33].

The increased Cr-content (Figures 5 and 6) in (Cu) and virtually unaffected Cr-particles in region R2 (Figure 1) lead to a presumed temperature range between 1175 °C (being the melting point of Cu

with 2.25 at % Cr in equilibrium) and below about 1800 °C (a homogenous liquid phase of Cu and Cr exist above 1800 °C). Due to the EDX measurements (Figure 6) it is expected that the Cr-content in R2 is slightly smaller than in R1. This further confirms a lower temperature in R2 compared to R1.

4. Conclusions

CuCr contact materials of two different compositions of 25 (CC75) and 43 wt % Cr (CC57) were investigated before and after a single current interruption in vacuum. The re-solidified microstructure after one current interruption consists of two regions. In summary, the following conclusions can be drawn:

(1) The Cu matrix in the initial state already incorporates a small amount of dissolved Cr in the range of 0.1–0.3 at %. This leads to a decreasing electrical conductivity of bulk material down to 21.7 MS/m (CC57) and 31.5 MS/m (CC75). These electrical conductivities can be estimated by applying the according Hashin-Shtrikman formula for Cr-particles incorporated in a Cr-enriched Cu solid solution matrix with reduced electrical conductivity.

(2) Region 1 contains fine Cr-particles and a Cu-Cr solid solution with about 2.25 at % Cr. Hence, the electrical conductivity of the contact material in this region is further reduced to 10 MS/m or lower. R1 also exhibits a common solidification texture with <001> in parallel to the solidification direction. Indicated by microstructure and texture formation, it can be concluded that both phases Cu and Cr being present in the as-manufactured state are considered to be liquid during the switching process. The temperature must be above 1800 °C during arcing and very high cooling rates between 4.5×10^4 K/s and 1.86×10^5 K/s are expected due to the small Cr-particle size of about 450 nm.

(3) Region 2 is characterized by large elongated Cu-grains (up to a length of 200 µm) perpendicularly aligned to the surface. The Cu-grains are still aligned with <001> in parallel to the solidification direction. In this region, only Cu is considered to be completely melted during interruption. The Cr-particles remain virtually unaffected when compared to the initial state. Therefore, it is concluded that the temperature in R2 was between 1175 °C and 1800 °C. This temperature is high enough to melt the Cu and still yields a Cu solid solution supersaturated with Cr.

(4) The total Cr-content of the contact materials showed only negligible influence on microstructure formation and resulting supersaturated Cr in Cu solid solution. However, the texturing during solidification is stronger for CC75, which might be caused by its higher thermal conductivity and therefore higher cooling rates during re-solidification when compared to CC57 material.

Acknowledgments: Alexander Kauffmann thanks the Carl-Zeiss-Foundation for financial support in the form of a postdoc grant. This work was partly carried out with the support of the Karlsruhe Nano Micro Facility (KNMF, www.knmf.kit.edu), a Helmholtz Research Infrastructure at Karlsruhe Institute of Technology (KIT, www.kit.edu). We gratefully acknowledge funding of the Bruker D8 through the Helmholtz Energy Materials Characterization Platform (HEMCP) initiated by the Helmholtz Association and coordinated by Forschungszentrum Jülich. Furthermore, we thank the Institute of Applied Materials Physics (IAM-AWP) at KIT, especially Judith Jung and Thomas Bergfeldt for performing the determination of temperature conductivity and ICP-OES analysis, respectively. Last but not least, we thank Nadira Hadžić and Pascal Schreiber for supporting sample preparation.

Author Contributions: Ulla Hauf, Alexander Kauffmann, Martin Heilmaier, Alexander Feilbach and Volker Hinrichsen conceived and designed the experiments; Ulla Hauf, Alexander Kauffmann, Sandra Kauffmann-Weiss and Alexander Feilbach performed the experiments; Ulla Hauf and Alexander Kauffmann analyzed the data; Mike Boening and Frank E. H. Muller contributed the investigated materials. Martin Heilmaier, Frank E.H. Muller and Volker Hinrichsen directed the research. All authors contributed to writing the paper.

Conflicts of Interest: The authors declare no conflict of interest.

References

1. Zeng, K.; Hämäläinen, M. Thermodynamic analysis of stable and metastable equilibria in the Cu-Cr system. *Calphad Comput. Coupling Phase Diagr. Thermochem.* **1995**, *19*, 93–104. [CrossRef]
2. Villars, P. (Ed.) *Inorganic Solid Phases*; Springer Materials (Online Database); Springer: Heidelberg, Germany, 2016; Available online: http://materials.springer.com/isp/phase-diagram/docs/c_0905743 (accessed on 18 April 2017).
3. Li, D.; Robinson, M.B.; Rathz, T.J. Measurements of liquidus temperatures in the Cu-Nb and Cu-Cr systems. *J. Phase Equilib.* **2000**, *21*, 136–140. [CrossRef]
4. Ivanchenko, V.G.; Filatova, O.N. Methods of study and properties of powder materials calculation of phase equilibria and thermodynamics properties of alloys of the Cr-Cu system. *Powder Metall. Met. Ceram.* **1996**, *35*, 167–172. [CrossRef]
5. Jacob, K.T.; Priya, S.; Waseda, Y. A thermodynamic study of liquid Cu-Cr alloys and metastable liquid immiscibility. *Z. Metallkd.* **2000**, *91*, 594–600.
6. Chakrabarti, D.J.; Laughlin, D.E. The Cr-Cu (chromium-copper) system. *Bull. Alloy Phase Diagr.* **1984**, *5*, 59–68. [CrossRef]
7. Slade, P.G. *The Vacuum Interrupter: Theory, Design and Application*; CRC Press: Boca Raton, FL, USA, 2008; ISBN 978-0849390913.
8. Schulman, M.B.; Slade, P.G. Sequential modes of drawn vacuum arcs between butt contacts for currents in the 1 kA to 16 kA range. *IEEE Trans. Compon. Packag. Manuf. Technol. Part A* **1995**, *18*, 417–422. [CrossRef]
9. Jüttner, B. Erosion craters and arc cathode spots in vacuum. *Akad. Wiss. DDR Zent. Elektronenphys.* **1978**, *108*, 25–48. [CrossRef]
10. Von Klinski-Wetzel, K.; Kowanda, C.; Rettenmaier, T.; Heilmaier, M.; Müller, F.E.H.; Hinrichsen, V. Correlation between microstructural features of the melt zone and switching behavior in CuCr contact material. In Proceedings of the 27th International Conference on Electrical Contacts, Dresden, Germany, 22–26 June 2014.
11. Hauf, U.; Feilbach, A.; Böning, M.; Heilmaier, M.; Hinrichsen, V.; Müller, F.E.H. Investigation of the heat affected volume of CuCr contact material for vacuum interrupters. In Proceedings of the 27th International Symposium on Discharges and Electrical Insulation in Vacuum, Suzhou, China, 18–23 September 2016.
12. Dullni, E.; Gentsch, D.; Shang, W.; Delachaux, T. Resistance increase of vacuum interrupters due to high-current interruptions. *IEEE Trans. Dielectr. Electr. Insul.* **2016**, *23*, 1–7. [CrossRef]
13. Rieder, W.F.; Schussek, M.; Glätzle, W.; Kny, E. The influence of composition and Cr particle size of Cu/Cr contacts on chopping current, contact resistance, and breakdown voltage in vacuum interrupters. *IEEE Trans. Compon. Hybrids Manuf. Technol.* **1989**, *12*, 273–283. [CrossRef]
14. Li, W.; Thomas, R.L.; Smith, R.K. Effects of Cr content on the interruption ability of CuCr contact materials. *IEEE Trans. Plasma Sci.* **2001**, *29*, 744–748.
15. Xiu, S.; Yang, R.; Xue, J.; Wang, J.X.; Wang, J.Y. Microstructure and properties of CuCr contact materials with different Cr content. *Trans. Nonferr. Met. Soc. China* **2011**, *21*, s389–s393. [CrossRef]
16. NIST-JANAF Thermochemical Tables. Available online: http://kinetics.nist.gov/janaf/ (accessed on 10 January 2017).
17. Feilbach, A.; Hauf, U.; Böning, M.; Hinrichsen, V.; Heilmaier, M.; Müller, F.E.H. Investigation of current breaking capacity of vacuum interrupters with focus on contact material properties with the help of a reference model vacuum circuit breaker. In Proceedings of the 27th International Symposium on Discharges and Electrical Insulation in Vacuum, Suzhou, China, 18–23 September 2016.
18. Bachmann, F.; Hielscher, R.; Schaeben, H. Texture analysis with MTEX—Free and open source software toolbox. *Solid State Phenom.* **2010**, *160*, 63–68. [CrossRef]
19. Wang, F.; von Klinski-Wetzel, K.; Mukherjee, R.; Nestler, B.; Heilmaier, M. Experimental and numerical investigation on the phase separation affected by cooling rates and marangoni convection in Cu-Cr alloys. *Metall. Mater. Trans. A* **2015**, *46*, 1756–1766. [CrossRef]
20. Sun, Z.; Wang, Y.; Guo, J. Liquid phase separation of Cu-Cr alloys during rapid cooling. *Trans. Nonferr. Met. Soc. China* **2006**, *16*, 998–1002. [CrossRef]
21. Kocks, U.F.; Tomé, C.N.; Wenk, H.R. *Texture and Anisotropy*; Cambridge University Press: Cambridge, UK, 2000; ISBN 0-521-79420-X.

22. Winegard, W.C. Fundamentals of the solidification of metals. *Metall. Rev.* **1961**, *21*, 57–99.
23. Suwas, S.; Ray, R.K. *Crystallographic Texture of Material*; Springer: London, UK, 2014; ISBN 978-1-4471-6313-8.
24. Ardakani, M.G.; Souza, N.D.; Wagner, A.; Shollock, B.A.; McLean, M. Competitive grain growth and texture evolution during directional solidification of superalloys. In Proceedings of the 9th International Symposium on Superalloys, Seven Springs, PA, USA, 17–21 September 2000; Pollock, T.M., Ed.; TMS: Warrendale, PA, USA, 2000; pp. 219–228.
25. Tenwick, M.J.; Davies, H.A. Enhanced strength in high conductivity copper alloys. *Mater. Sci. Eng.* **1988**, *98*, 543–546. [CrossRef]
26. Bell, A.; Davies, H.A. Solid solubility extension in Cu-V and Cu-Cr alloys produced by chill block melt-spinning. *Mater. Sci. Eng. A* **1997**, *226–288*, 1039–1041. [CrossRef]
27. Straumanis, M.E.; Yu, L.S. Lattice parameters, densities, expansion coefficients and perfection of structure of Cu and of Cu-In α phase. *Acta Crystallogr. Sect. A* **1969**, *25*, 676–682. [CrossRef]
28. Haynes, W.M. (Ed.) *Handbook of Chemistry and Physics*, 96th ed.; CRC Press: Boca Raton, FL, USA, 2015.
29. Hashin, Z.; Shtrikman, S. A variational approach to the theory of the effective magnetic permeability of multiphase materials. *J. Appl. Phys.* **1962**, *33*, 3125–3131. [CrossRef]
30. Von Klinski-Wetzel, K.; Kowanda, C.; Heilmaier, M.; Müller, F.E.H. The influence of microstructural features on the electrical conductivity of solid phase sintered CuCr composites. *J. Alloy. Compd.* **2015**, *631*, 237–247. [CrossRef]
31. Villars, P. (Ed.) *Inorganic Solid Phases*; Springer Materials (Online Database); Springer: Heidelberg, Germany, 2016; Available online: http://materials.springer.com/isp/phase-diagram/docs/c_0908235 (accessed on 26 May 2017).
32. Methling, R.; Franke, St.; Gortschakow, S.; Abplanalp, M.; Sütterlin, R.P.; Delachaux, T.; Menzel, K.O. Comparison of methods of electrode temperature determination in high-current vacuum arcs. In Proceedings of the 27th International Symposium on Discharges and Electrical Insulation in Vacuum, Suzhou, China, 18–23 September 2016.
33. Pieniak, T.; Kurrat, M.; Gentsch, D. Surface temperature measurement of transversal magnetic field contacts using a thermography camera. In Proceedings of the 27th International Symposium on Discharges and Electrical Insulation in Vacuum, Suzhou, China, 18–23 September 2016.

© 2017 by the authors. Licensee MDPI, Basel, Switzerland. This article is an open access article distributed under the terms and conditions of the Creative Commons Attribution (CC BY) license (http://creativecommons.org/licenses/by/4.0/).